JOURNAL OF COMPUTATIONAL PHYSICS **132,** 327–345 (1997)
ARTICLE NO. CP965639

Computational Methods for Self-similar Solutions of the Compressible Euler Equations

Ravi Samtaney[1]

Graduate Aeronautical Laboratories and Applied Mathematics, Firestone Flight Sciences Laboratory, California Institute of Technology, Pasadena, California 91125
E-mail: ravi@ama.caltech.edu

Received April 17, 1996; revised December 12, 1996

Computations of self-similar solutions of the compressible Euler equations as a boundary value problem in similarity coordinates ($\xi = x/t$, $\eta = y/t$) are presented. Two new implicit methods namely the implicit Godunov method and the implicit Equilibrium Flux Method are presented. The Jacobians for the implicit methods are analytically evaluated. In general the self-similar solutions exhibit sharper discontinuities than corresponding solutions of the initial value problem. © 1997 Academic Press

I. INTRODUCTION

Many physical systems are mathematically approximated as systems of hyperbolic conservation laws. A common example, and one that will be dealt with at length in this paper, is the inviscid compressible flow of a gas for which the governing equations are the compressible Euler equations. Considerable work has been undertaken to study the refraction of a shock at a gaseous interface (see, for example, work of Henderson *et al.* [1] who investigated the transition from regular to irregular refraction). Another problem which has been the focus of several studies is the transition from regular to Mach reflection of a shock at a solid wedge (see, for example, the review paper by Hornung [2]). One common feature of both the shock-refraction and the shock-reflection problems is that the solution depends only upon $(x/t, y/t)$. Such solutions have been referred to as "pseudo-stationary" solutions of the Euler equations because they are fixed points of the partial differential equations resulting from a self-similar transformation of the Euler equations (see, for example, Refs. [1–5]). Another example of a self-similar flow is that of shock-diffraction around a right angle corner.

The solution to self-similar flows is typically obtained by solving the compressible Euler equations numerically as an *initial value problem* with appropriate boundary conditions. In this paper, we seek the self-similar solutions of the compressible Euler equations as a *boundary value problem* after a suitable self-similar transformation is made. The self-similar transformation reduces the number of independent variables by one. The solution we seek is a steady solution in the $(\xi \equiv x/t, \eta \equiv y/t)$ space. We believe that, intuitively, it is easier to deal with a steady state solution than one which is time-dependent. In addition, many of the test problems in the literature on numerical methods of Euler equations have self-similar solutions. The most commonly used test problem is the one-dimensional Sod's shock-tube problem [6], the solution of which is self-similar in the variable $\xi \equiv x/t$.

In this paper, the discretized form of the self-similar equations are solved using two methods: one seeks the steady state by an implicit method while the other is a fixed point iteration method. The numerical fluxes are evaluated using either the Equilibrium Flux Method (EFM) method [7] or the Godunov method [8]. Note that implicit methods usually involve two major operations: the solution of a linear system of equations is one while the other one is the evaluation of the flux Jacobians. In this paper, the Jacobians for the implicit method are evaluated analytically for the EFM and the Godunov method.

The outline of the paper is as follows. In Section II we present the Euler equations in self-similar form and classify these. In Section III we present two methods to obtain the self-similar solution numerically. In Section IV we present the following one-dimensional examples (for which the self-similar solutions exist): (a) Sod's shock-tube problem, (b) a nonlinearizable Riemann problem, and (c) the shock interaction with a contact discontinuity. The following two-dimensional examples are presented in Section V: (a) the shock reflection at a solid ramp, and (b) the shock refraction at a gaseous interface. The details of derivations of the Jacobians for the implicit methods are relegated to Appendixes A and B.

[1] Present address: MS T27A, MRJ Inc., NASA Ames Research Center, Moffett-Field, CA 94035-1000.

0021-9991/97 $25.00

II. SELF-SIMILAR FORMULATION

A. *General Formalism*

Consider a system of hyperbolic conservation laws,

$$\frac{\partial U}{\partial t} + \frac{\partial \mathscr{F}_i(U)}{\partial x_i} = 0, \tag{1}$$

$U \equiv U(x_i, t): \mathscr{R}^m \times \mathscr{R} \to \mathscr{R}^n$, and $\mathscr{F}_i(U): \mathscr{R}^n \to \mathscr{R}^n$. We seek solutions of the form $\tilde{U}(\xi_i) \equiv U(x_i, t)$ such that $\xi_i \equiv x_i/(Vt) \in \mathscr{R}^m$. Under the transformation $\xi_i \equiv x_i/t$ ($V \equiv 1$ without loss of generality), Eq. (1) reduces to

$$m\tilde{U} + \frac{\partial \tilde{\mathscr{F}}_i(\tilde{U}, \xi_i)}{\partial \xi_i} = 0, \tag{2}$$

where $\tilde{\mathscr{F}}_i(\tilde{U}, \xi_i) \equiv \mathscr{F}_i(\tilde{U}) - \xi_i \tilde{U}$.

B. *Compressible Euler Equations*

Consider the compressible Euler equations in two space dimensions written below in conservation form

$$U_t + F_x(U) + G_y(U) = 0, \tag{3}$$

where

$$\begin{aligned} U(x, y, t) &= \{\rho, \rho u, \rho v, E\}^T, \\ F(U) &= \{\rho u, \rho u^2 + p, \rho uv, (E + p)\, u\}^T, \\ G(U) &= \{\rho v, \rho uv, \rho v^2 + p, (E + p)v\}^T, \end{aligned} \tag{4}$$

where ρ is the density, (u, v) is the velocity vector, p is the pressure, and E is the total energy per unit volume. We assume a perfect gas equation of state throughout the paper and thus close the above set of partial differential equations by the relation

$$p = (\gamma - 1)\left(E - \frac{1}{2}\rho(u^2 + v^2)\right), \tag{5}$$

where γ is the ratio of specific heats of the gas. For simplicity γ is assumed constant in space and time, and is set to 1.4.

Under the similarity transformation ($\xi \equiv x/t$, $\eta \equiv y/t$), Eq. (3) transforms to

$$2\tilde{U} + \tilde{F}_\xi + \tilde{G}_\eta = 0, \tag{6}$$

where

$$\begin{aligned} \tilde{F} &= \{\rho(u - \xi), \rho u(u - \xi) + p, \rho(u - \xi)v, E(u - \xi) + pu\}^T, \\ \tilde{G} &= \{\rho(v - \eta), \rho u(v - \eta), \rho v(v - \eta) + p, E(v - \eta) + pv\}^T. \end{aligned} \tag{7}$$

Note that $\tilde{F}$ (or $\tilde{G}$) is equivalent to the flux of mass, momentum, and energy through a surface locally moving with a speed of ξ (or η).

C. *Classification of the Self-similar PDEs*

For the purposes of classifying the self-similar partial differential equations (Eq. 6) it is convenient to rewrite the compressible Euler equations in non-conservation form as

$$V_t + AV_x + BV_y = 0, \tag{8}$$

$$V = \{\rho, u, v, p\}^T. \tag{9}$$

The matrices A and B are

$$A = \begin{bmatrix} u & \rho & 0 & 0 \\ 0 & u & 0 & \frac{1}{\rho} \\ 0 & 0 & u & 0 \\ 0 & \gamma p & 0 & u \end{bmatrix}, \qquad B = \begin{bmatrix} v & 0 & \rho & 0 \\ 0 & v & 0 & 0 \\ 0 & 0 & v & \frac{1}{\rho} \\ 0 & 0 & \gamma p & v \end{bmatrix}. \tag{10}$$

After the self-similar transformation Eq. (8) reduces to

$$(A - I\xi)V_\xi + (B - I\eta)V_\eta = 0. \tag{11}$$

Assuming $(A - I\xi)$ to be non-singular, we obtain the quasi-linear form

$$V_\xi + (A - I\xi)^{-1}(B - I\eta)V_\eta = 0. \tag{12}$$

The four eigenvalues of $(A - I\xi)^{-1}(B - I\eta)$ are

$$\lambda_{1,2} = \frac{\tilde{v}}{\tilde{u}}, \qquad \lambda_{3,4} = \frac{\tilde{u}\tilde{v} \pm c(\tilde{u}^2 + \tilde{v}^2 - c^2)^{1/2}}{\tilde{u}^2 - c^2}, \tag{13}$$

where $u = u - \xi$ and $v = v - \eta$, and $c^2 = \gamma p/\rho$ defines the sound speed. We define a self-similar Mach number as

$$\tilde{M}^2 = \frac{(\tilde{u}^2 + \tilde{v}^2)}{c^2}. \tag{14}$$

If $\tilde{M} < 1$ (≥ 1) then the eigenvalues $\lambda_{3,4}$ are complex conjugates (real). This implies that the system of equations (Eq. 6) is of the *mixed hyperbolic-elliptic* type.

III. NUMERICAL METHODS TO SOLVE THE SELF-SIMILAR PDES

In this section, we present two methods to solve Eq. (6) numerically. The first method is an implicit method (a la Newton–Raphson) while the second one is a fixed point iteration method (a la Jacobi).

The domain, $\Omega \equiv [\xi_l, \xi_r] \times [\eta_l, \eta_r]$, is divided into a uniform grid with each computational zone of area $\Delta\xi \times \Delta\eta$. The size of the grid is $N \times M$ such that $N = (\xi_r - \xi_l)/\Delta\xi$ and $M = (\eta_r - \eta_l)/\Delta\eta$. The requirement of a uniform grid is not strict and the methods are easily extensible to stretched grids.

A. *Implicit Method*

The discrete form for Eq. (6) is written at iteration $n + 1$ as (dropping the $\sim$ over U, F, and G)

$$2U_{i,j}^{n+1} + \frac{F_{i+1/2,j}^{n+1} - F_{i-1/2,j}^{n+1}}{\Delta\xi} + \frac{G_{i,j+1/2}^{n+1} - G_{i,j-1/2}^{n+1}}{\Delta\eta} = 0, \quad (15)$$

where $i = 1, ..., N$, $j = 1, ..., M$, and $U_{i,j} \equiv U(\xi_i, \eta_j)$ is the numerical approximation to the exact solution $U(\xi, \eta)$ of the system of partial differential equations (Eq. (6)). Furthermore, $U_{i,j}$ is the cell average of the numerical solution in the cell (i, j) which covers a domain $[\xi_{i-1/2}, \xi_{i+1/2}] \times [\eta_{j-1/2}, \eta_{j+1/2}]$ and whose geometric center is given by (ξ_i, η_j).

We develop the method further for a flux function of the type $F \equiv F(U_L, U_R)$, i.e., the flux in the ξ direction depends on the left and right states at the cell interface. Examples of such flux functions include EFM, Godunov method, Roe method [9], etc. In this paper, we focus on the Godunov and the EFM methods.

We now assume that the left and right states at a cell interface are obtained by fitting linear profiles in each direction in each cell and applying monotonicity constraints (see Appendix C for details of the linear reconstruction procedure). The slopes for the linear profiles are a function of the cell average values in the cell and its neighbors. The linear reconstruction procedure makes the solution formally second order accurate. Alternatively one may use the piecewise parabolic method [10] or the essentially non-oscillatory reconstruction procedures [11]. The linear reconstruction gives the left and right states at the cell interface $\xi_{i+1/2}$ as

$$\begin{aligned} U_{L,i+1/2,j} &= U_{i,j} + \left(\frac{\partial U}{\partial \xi}\right)_{i,j} \frac{\Delta\xi}{2}, \\ U_{R,i+1/2,j} &= U_{i+1,j} - \left(\frac{\partial U}{\partial \xi}\right)_{i+1,j} \frac{\Delta\xi}{2}, \end{aligned} \quad (16)$$

and the left and right states at the cell interface $\eta_{j+1/2}$ are

$$\begin{aligned} U_{L,i,j+1/2} &= U_{i,j} + \left(\frac{\partial U}{\partial \eta}\right)_{i,j} \frac{\Delta\eta}{2}, \\ U_{R,i,j+1/2} &= U_{i,j+1} - \left(\frac{\partial U}{\partial \eta}\right)_{i,j+1} \frac{\Delta\eta}{2}. \end{aligned} \quad (17)$$

Therefore, the flux functions at the cell interfaces $\xi_{i+1/2}$ and $\eta_{j+1/2}$ may be written as

$$\begin{aligned} F_{i+1/2,j}^{n+1} &\equiv F(U_{L,i+1/2,j}^{n+1}, U_{R,i+1/2,j}^{n+1}), \\ G_{i,j+1/2}^{n+1} &\equiv G(U_{L,i,j+1/2}^{n+1}, U_{R,i,j+1/2}^{n+1}). \end{aligned} \quad (18)$$

A Taylor series expansion yields

$$F_{i+1/2,j}^{n+1} = F_{i+1/2,j}^{n} + \left(\frac{\partial F}{\partial U_L}\right)_{i+1/2,j}^{n} \delta U_{L,i+1/2,j}^{n} + \left(\frac{\partial F}{\partial U_R}\right)_{i+1/2,j}^{n} \delta U_{R,i+1/2,j}^{n} + \cdots, \quad (19)$$

$$G_{i+1/2,j}^{n+1} = G_{i,j+1/2}^{n} + \left(\frac{\partial G}{\partial U_L}\right)_{i,j+1/2}^{n} \delta U_{L,i,j+1/2}^{n} + \left(\frac{\partial G}{\partial U_R}\right)_{i,j+1/2}^{n} \delta U_{R,i,j+1/2}^{n} + \cdots, \quad (20)$$

where

$$\begin{aligned} \delta U_{K,l}^{n} &= U_{K,l}^{n+1} - U_{K,l}^{n}, \\ K &= L, R, \; l = (i + 1/2, j), (i, j + 1/2). \end{aligned} \quad (21)$$

Denote the Jacobians of the fluxes F and G in Eq. (20) as

$$\begin{aligned} A_{K,i\pm1/2,j} &= \left(\frac{\partial F}{\partial U_K}\right)_{i\pm1/2,j}, \\ B_{K,i,j\pm1/2} &= \left(\frac{\partial G}{\partial U_K}\right)_{i,j\pm1/2}, K = L, R. \end{aligned} \quad (22)$$

We choose the following flux functions: (a) the Godunov method in which the exact one-dimensional nonlinear Riemann problem is solved at each cell interface and (b) the Equilibrium Flux Method. For the choice (a) above the method is referred to as the *implicit Godunov method*; and for (b) the method may be referred to as the *implicit Equilibrium Flux Method.* The derivations of the Jacobians (Eq. (22)) for the implicit Godunov method and the implicit Equilibrium Flux Method are given in Appendixes A and B, respectively.

Using Eqs. (20), (16), (17), (21), and (15) we obtain

$$\begin{aligned} 2\delta U^n_{i,j} &+ (A^n_{L,i+1/2,j} - A^n_{R,i-1/2,j} + B^n_{L,i,j+1/2} - B^n_{R,i,j-1/2})\,\delta U^n_{i,j} \\ &- A^n_{L,i-1/2,j}\delta U^n_{i-1,j} + A^n_{R,i+1/2,j}\delta U^n_{i+1,j} - B^n_{L,i,j-1/2}\delta U^n_{i,j-1} \\ &+ B^n_{R,i,j+1/2}\delta U^n_{i,j+1} + \mathscr{S} = \mathscr{R}^n_{i,j}. \end{aligned} \tag{23}$$

The term $\mathscr{S}$ solely contains the terms involving the slopes which are used to obtain the linear profile in the cell and is given by

$$\begin{aligned} 2\mathscr{S} &= (A^n_{L,i+1/2,j} + A^n_{R,i-1/2,j})\,\delta^n\left(\frac{\partial U}{\partial \xi}\right)_{i,j} \\ &- A^n_{L,i-1/2,j}\,\delta^n\left(\frac{\partial U}{\partial \xi}\right)_{i-1,j} - A^n_{R,i+1/2,j}\,\delta^n\left(\frac{\partial U}{\partial \xi}\right)_{i+1,j} \\ &+ (B^n_{L,i,j+1/2} + B^n_{R,i,j-1/2})\,\delta^n\left(\frac{\partial U}{\partial \eta}\right)_{i,j} \\ &- B^n_{L,i,j-1/2}\,\delta^n\left(\frac{\partial U}{\partial \eta}\right)_{i,j-1} - B^n_{R,i,j+1/2}\,\delta^n\left(\frac{\partial U}{\partial \eta}\right)_{i,j+1}, \end{aligned} \tag{24}$$

where

$$\delta^n\left(\frac{\partial U}{\partial \zeta}\right)_{i,j} = \left(\frac{\partial U}{\partial \zeta}\right)^{n+1}_{i,j} - \left(\frac{\partial U}{\zeta}\right)^{n}_{i,j}, \qquad \zeta = \xi, \eta. \tag{25}$$

For a first order method $\mathscr{S}$ vanishes identically. For a formally second order accurate method $\mathscr{S}$ contains terms involving the slope at the $(n+1)$st and the nth iteration. For example, the slope in the ξ direction in the $(i-1, j)$th cell is a complicated function of $U_{i-k,j}$, $k = 2, 1, 0$, which incorporates some form of slope-limiting (the exact slope fitting procedure is given in Appendix C). For simplicity, in our formulation we set $\mathscr{S} = 0$. This enables us to write the left hand side of Eq. (23) as a product of a block penta-diagonal matrix and the vector of unknowns δU^n. We rationalize that at convergence the change in slopes from the nth to the $(n+1)$st iterations would be zero.

The right hand side of Eq. (23), $\mathscr{R}^n_{i,j}$, is the residual and is simply the discrete approximation to the partial differential equations at iteration n, i.e.,

$$\mathscr{R}^n_{i,j} = 2U^n_{i,j} + \frac{F^n_{i+1/2,j} - F^n_{i-1/2,j}}{\Delta\xi} + \frac{G^n_{i,j+1/2} - G^n_{i,j-1/2}}{\Delta\eta}. \tag{26}$$

In other words, at each iterate, the system of equations we solve is

$$\mathscr{A}^n \delta U^n = \mathscr{R}^n, \tag{27}$$

where $\mathscr{A}$ is a block penta-diagonal matrix of size $NM \times NM$ and each block is a 4×4 matrix. The vector δU^n is the vector of NM unknowns (and each unknown is a vector of 4 components) and is given by

$$\begin{aligned} \delta U^n = (&\delta U^n_{1,1}, \delta U^n_{2,1}, \cdots, \delta U^n_{N,1}, \\ &\delta U^n_{1,2}, \cdots, \delta U^n_{N,2}, \cdots, \delta U^n_{1,M}, \cdots, \delta U^n_{N,M})^T. \end{aligned} \tag{28}$$

$\mathscr{R}$ is the residual vector of size NM and each component of $\mathscr{R}$ is a vector of four components. A direct inversion of $\mathscr{A}^n$ is impractical. Moreover for simplicity of parallel implementation we adopt the following strategy. We multiply Eq. (27) by $\omega(\ll 1)$ and add the term $\delta U^{n+1} = 0$. Finally we approximate, $\delta U^{n+1} \approx \delta U^n$ which is reasonable when we are near convergence. Thus we have

$$(I + \omega\mathscr{A}^n)\,\delta U^n = \omega\mathscr{R}^n, \tag{29}$$

where $(I + \omega\mathscr{A}^n)$ is also a block penta-diagonal matrix. The left hand side of Eq. (29) is now approximated as a product of two block tri-diagonal matrices as

$$(I + \omega\mathscr{A}^n_x)(I + \omega\mathscr{A}^n_y)\,\delta U^n = \omega\mathscr{R}^n, \tag{30}$$

i.e., we used $(I + \omega\mathscr{A}) = (I + \omega\mathscr{A}_x)(I + \omega\mathscr{A}_y) + O(\omega^2)$. The solution procedure for block tri-diagonal linear systems is a well known algorithm and a discussion of this is omitted in the interest of brevity. We solve the two block tri-diagonal systems in succession and obtain the solution vector δU^n. To monitor convergence we compute the L_∞ norm of $\mathscr{R}$. The convergence criterion is

$$\|\mathscr{R}\|_\infty < \varepsilon \approx 10^{-10}.$$

B. *Fixed Point Iteration Method*

Due to the inherent complications in the implicit method, such as those involved in the evaluation of the Jacobians and inversion of matrices, it may be preferable in certain instances to solve the equations in an explicit manner. A fixed point iteration method is outlined below.

The partial differential equations (Eq. (6)) are discretized as

$$\alpha U^{n+1} + \beta U^n = \left(\frac{F^n_{i+1/2,j} - F^n_{i-1/2,j}}{\Delta\xi} + \frac{G^n_{i,j+1/2} - G^n_{i,j-1/2}}{\Delta\eta}\right), \tag{31}$$

such that $\alpha + \beta = 2$. Rewriting it explicitly we obtain

$$\begin{aligned} U^{n+1} = &-\frac{\beta}{\alpha}U^n - \frac{1}{\alpha} \\ &\left(\frac{F^n_{i+1/2,j} - F^n_{i-1/2,j}}{\Delta\xi} + \frac{G^n_{i,j+1/2} - G^n_{i,j-1/2}}{\Delta\eta}\right). \end{aligned} \tag{32}$$

We iterate until the residual $\mathscr{R}$ (the same as in the implicit method) meets the convergence criteria. Although, the main advantage of this method is its simplicity, the disadvantages could be either a very slow convergence to the solution or a complete lack of convergence. The lack of convergence may occur if the fixed point iteration technique goes in to a limit cycle. The exact conditions when the fixed point iteration fails to converge are not known. It is possible that a different initial guess may mitigate this problem. For fixed point iteration techniques it is known that the magnitude of the Jacobian of the right hand side of Eq. (32) must be less than unity. This places a restriction on the values of α and β.

C. *Parallel Implementation*

Both the implicit and the fixed point iteration technique were implemented on the 512-node Intel Paragon at Caltech. The domain decomposition is achieved by slicing the domain in the η direction, i.e., the solution vector U is distributed row-wise. For the implicit method, we solve Eq. (30) as

$$(I + \omega \mathscr{A}_x)^n \, \delta U^* = \omega \mathscr{R}^n. \tag{33}$$

This linear block tri-diagonal system is solved using the Intel library routines. After the vector δU^* is obtained on each processor we distribute it column-wise (denote the rearranged vector $(\delta U^*)^T$) and then solve the equation

$$(I + \omega \mathscr{A}_y)^n \, \delta U^n = (\delta U^*)^T. \tag{34}$$

We adopted the NX message passing library for the Intel paragon. The ease of solving the block tri-diagonal systems was instrumental in using the decomposition of the block-penta-diagonal system in Eq. (30). A ghost boundary was implemented for each array distributed on each processor. For the implicit methods, each processor communicates data with every other processor. The communications were essentially done in an asynchronous fashion to avoid communication delays. Of course, for the fixed point iteration technique we did not have to invert the block penta-diagonal matrix and the communication involved only the ghost boundaries. In other words, the explicit method involved only nearest neighbor communications.

For the two-dimensional example of shock refraction presented in Section V-B, the execution time on the Intel Paragon is shown in Table I. The number in the bracket next to the execution time is speed-up which is normalized to unity for four processors. The ratio of execution time for the implicit Godunov method to the explicit Godunov method varied from 2.6 to 2.8 while the ratio of execution time for the implicit EFM to the explicit EFM varied from 3.1 to 3.4. One technique to decrease the execution time for the implicit methods is to freeze the Jacobians and recalculate them every ''n'' iterations where typically $n = 5, 10$.

IV. ONE-DIMENSIONAL EXAMPLES

In one dimensions, the self-similar equations (Eq. (6)) reduce to ordinary differential equations. Although in the previous section we focused on developing the methods in two dimensions, the implementation of the above methods in one dimension is straightforward. For the implicit method in one dimension, we invert a block tri-diagonal system only. When we are close to convergence, the parameter ω can be made very large and thus the method reduces to a Newton–Raphson method.

For some examples, we present comparisons of the self-similar computations with solutions obtained by solving the corresponding initial-value problem, i.e., solutions of Eq. (3). These solutions are obtained by a second-order accurate in space and time Godunov method or EFM. The second order accuracy in space is obtained by the same linear reconstruction used for the self-similar calculations. The time marching procedure is a second order accurate Runge–Kutta time integration. The fluxes for the Godunov method are obtained by solving a one-dimensional Riemann problem at each cell interface [8]. For EFM, the flux at a cell interface is calculated as in the Appendix B but with $\xi = 0$.

TABLE I

Execution Times for 100 Iterations for the Self-similar Solution of the Two-Dimensional Shock-Refraction Problem on a 192×96 Mesh

No. processors	Explicit EFM	Implicit EFM	Explicit Godunov	Implicit Godunov
4	124 (1.00)	420 (1.00)	179 (1.00)	504 (1.00)
8	65 (1.91)	212 (1.98)	96 (1.86)	265 (1.90)
16	35 (3.54)	109 (3.85)	51 (3.51)	137 (3.68)
32	19 (6.53)	60 (7.00)	28 (6.39)	74 (6.81)

Note. The execution time is given in seconds for the Intel Paragon. The number in the bracket is the speed-up which is normalized to unity for four processors.

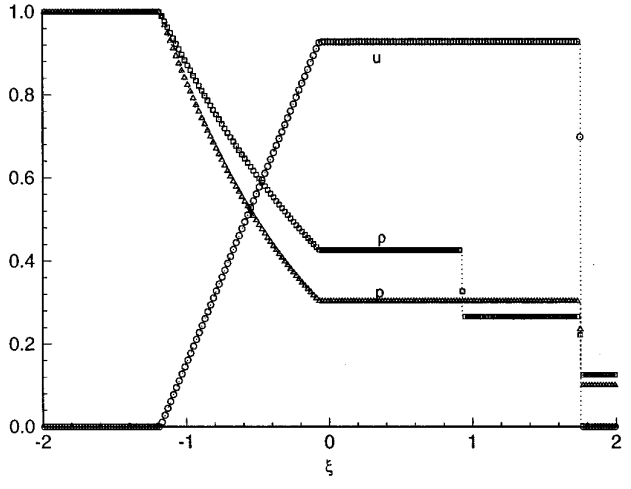

FIG. 1. Self-similar solution for Sod's shock-tube problem. The dotted line is the analytical solution, while the symbols denote the numerical solution (implicit Godunov method).

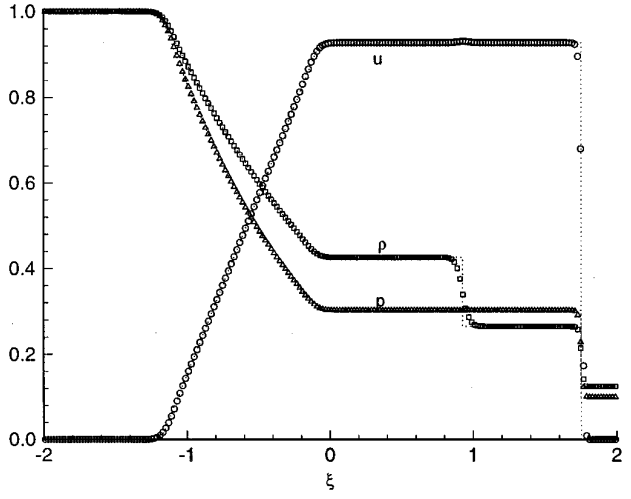

FIG. 3. Self-similar solution for Sod's shock-tube problem. The dotted line is the analytical solution, while the symbols denote the numerical solution (implicit EFM).

A. *Sod's Shock-Tube Problem*

Sod's shock-tube problem is considered as one of the standard tests of a numerical method for compressible Euler equations [6]. In this problem, the initial conditions in the gas are

$$(\rho, u, p) = \begin{cases} (1, 0, 1) & \forall\, x < 0 \\ (0.125, 0, 0.1) & \forall\, x > 0. \end{cases} \tag{35}$$

The solution to this problem is a self-similar solution consisting of a shock wave, a contact discontinuity, and a rarefaction. The results are plotted in Fig. 1. This problem has an analytical solution and the self-similar solution reproduces the analytical solution accurately. An added advantage of the solution in self-similar form is that the wave velocities are equal to the coordinate ξ and can be easily obtained from the plot; for example, we observe that the shock and contact speeds are 1.75 and 0.92, respectively. The self-similar solution was also computed using the implicit EFM method. The results are plotted in Fig. 3.

In actual practice, the residual at each point has three components, one each for the continuity, momentum, and energy equations. The L_∞ norm of the residual for the continuity and the energy equations is plotted in Fig. 2 and Fig. 4 for the implicit Godunov and the implicit EFM

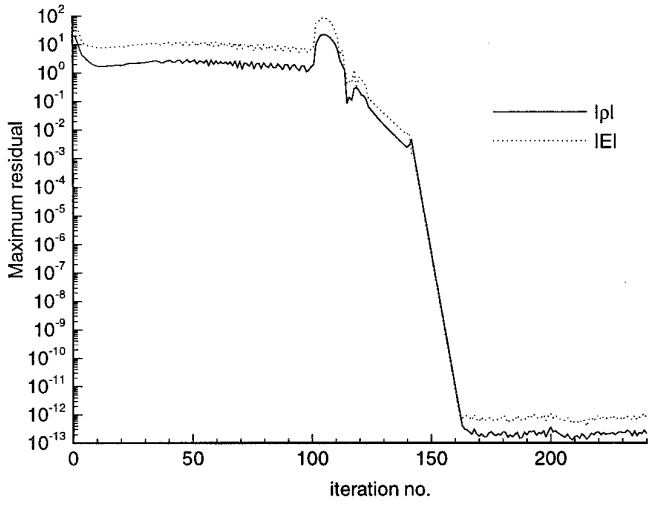

FIG. 2. Residual for Sod's shock-tube problem using implicit Godunov method.

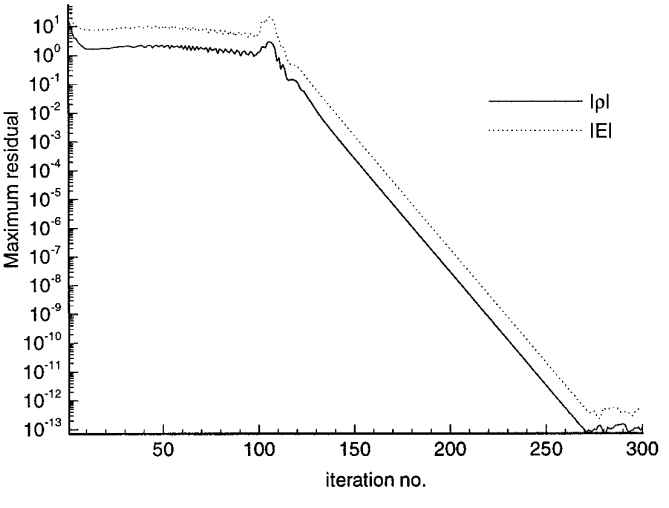

FIG. 4. Residual for Sod's shock-tube problem using implicit EFM.

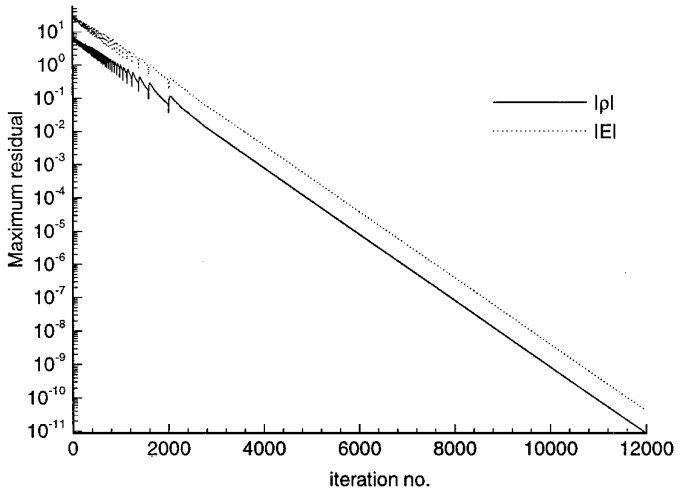

FIG. 5. Residual for Sod's shock-tube problem using the fixed point iteration technique. The fluxes were calculated by the Godunov method.

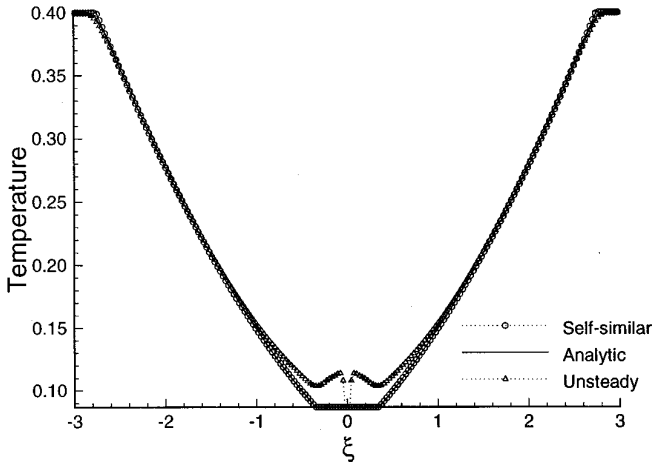

FIG. 6. Self-similar solution for the non-linearizable Riemann problem using the implicit Godunov method.

method, respectively. The L_∞ norm is less than 10^{-10} at the last iteration and thus the discrete approximations of the self-similar form of the continuity and the energy equations were satisfied to nearly machine precision. The value of ω was chosen as 0.001 for the first few iterations and was increased during the computation. The same problem was computed using the fixed point iteration scheme and using the Godunov method to compute the fluxes. The results are identical to those in Fig. 1 and hence omitted. The convergence history (Fig. 5) clearly indicates that while the fixed point iteration scheme may be simpler to implement, it suffers from extremely slow convergence even for this simple problem.

B. *Nonlinearizable Riemann Problem*

Another example which tests the robustness of the method is the solution of the Riemann problem with the initial conditions

$$(\rho, u, p) = \begin{cases} (1, -2, 0.4) & \forall x < 0 \\ (1, 2, 0.4) & \forall x > 0. \end{cases} \tag{36}$$

According to a proposition by Einfeldt *et al.* (Proposition 3.1 in [12]), if the following conditions are satisfied

$$\frac{4\gamma\rho E}{3\gamma - 1} - (\rho u)^2 > 0, \qquad (\gamma - 1)\rho E - (\rho u)^2 \leq 0 \tag{37}$$

then the Riemann problem has a solution with positive density and internal energy but is nonlinearizable. Therefore, this a stringent test and numerical methods relying on the solution of a linearized Riemann problem (for example, the Roe method [9]) fail to provide a solution. However, it must be noted that the Roe method with an entropy fix does provide a solution. The solution to this problem is a self-similar solution and consists of two rarefaction waves, one moving to the left and the other moving to the right. Furthermore, this solution can be determined analytically. The solution to the initial-value problem (Eq. (3)) was computed by a second order space and time accurate Godunov method until time $t = 1$. The temperature in the self-similar solution, solution to the initial-value problem at $t = 1$, and the analytical solution are plotted in Fig. 6. Good agreement between the self-similar and the analytical solutions is observed, and we note that the self-similar solution reproduces the slope discontinuity at the head and tail of the rarefaction quite accurately. On the other hand, the solution to the initial-value problem exhibits a numerical artifact in the center of the domain and also the slope

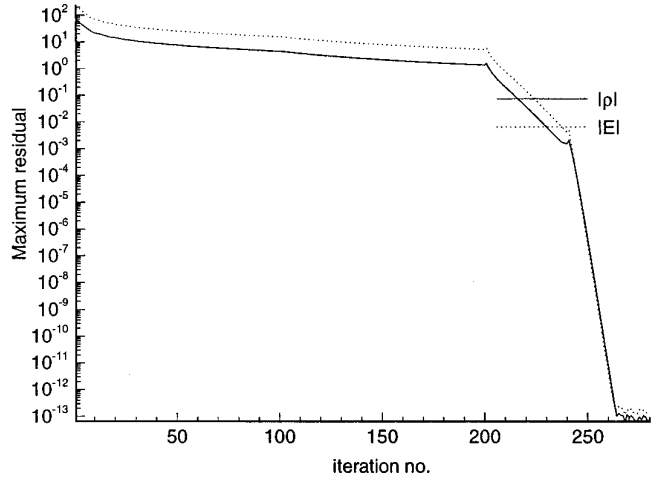

FIG. 7. Residual for the non-linearizable Riemann problem using the implicit Godunov method.

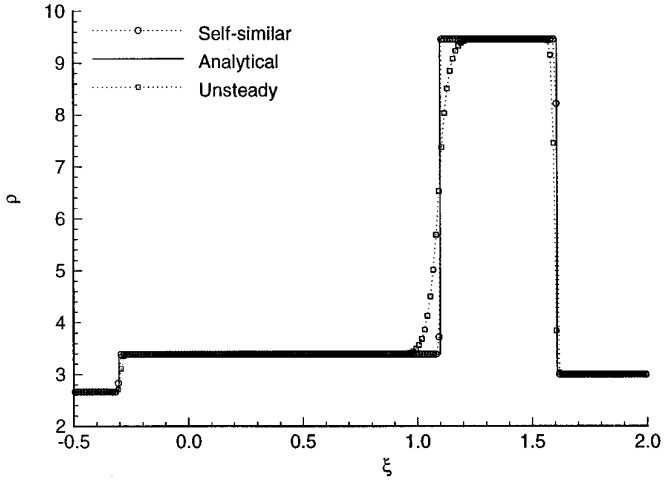

FIG. 8. Self-similar solution for a 1D shock contact interaction using the implicit Godunov method.

discontinuity is smoothed out. The convergence history for the self-similar computation is plotted in Fig. 7.

C. *One-Dimensional Shock Contact Interaction*

In this section we present the results of a one-dimensional shock contact interaction. We initialize a stationary contact-discontinuity at $x = 0$ with density $\rho = 1$ ($\rho = 3$) for $x < 0$ ($x > 0$). This contact is hit by a shock moving from left to right with a shock Mach number $M = 1.5$. At $t = 0$ the shock hits the contact-discontinuity and undergoes refraction. The reflected and the transmitted waves are both shocks in this case. The solution to this problem is also self-similar and in fact the Euler equations can be reduced to a set of algebraic equations which can be solved to yield the analytical solution [13]. The numerical self-similar solution and the solution at $t = 1$ of the initial-value problem are plotted in Fig. 8. In this case the contact discontinuity is sharper in the self-similar solution than the solution of the initial value problem. Agreement between the self-similar and the analytical solutions is observed. The L_∞ norm of the residual is plotted in Fig. 9.

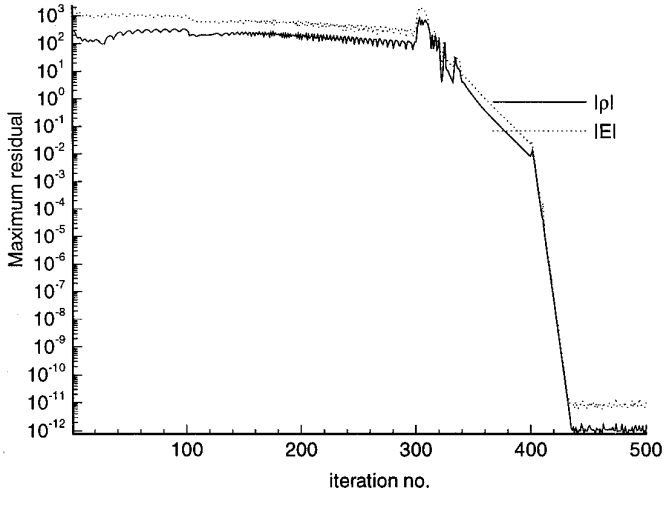

FIG. 9. Residual for the shock-contact problem using the implicit Godunov method.

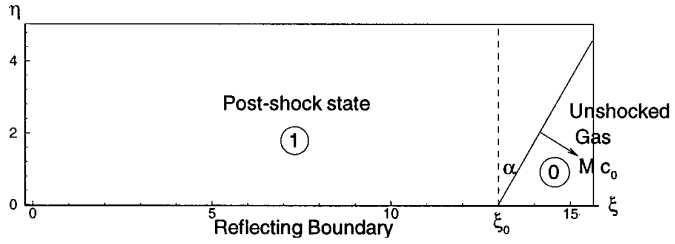

FIG. 10. Initial guess and boundary conditions for an $M = 9.5$ shock reflection at a $\alpha = 30°$ wedge.

V. TWO-DIMENSIONAL EXAMPLES

A. *Shock-Reflection*

Presently we consider the problem of a strong shock reflection at a solid wedge. The shock Mach number is $M = 9.5$ and the wedge angle is $\alpha = 30°$. This problem is very similar to that considered by Berger and Colella [14] except in their case the Mach number was $M = 10$. The domain, $\Omega = [0, 15.625] \times [0, 5]$ is discretized by a mesh of size 512×256. The mesh spacing in the η direction was uniform while in the ξ direction it was uniform over a domain [10.625, 15.625] and then geometrically stretched in the domain [0, 10.625]. In Fig. 10, we show the initial guess of the solution and boundary conditions. The shock moves at a speed Mc_0 where c_0 is the sound speed in the unshocked gas. The shock is initialized as a straight line given by $\xi - \xi_0 = \eta \tan \alpha$ where $\xi_0 = Mc_0/\cos(\alpha)$. The conditions behind the shock are indicated by 1 and are obtained by the Rankine–Hugoniot jump conditions.

Since the initial guess was far from the actual solution, initially we use a small value of the iteration parameter $\omega = 0.001$. This parameter is tunable and at the end of the simulation this could be increased to $\omega = 0.005$. For coarser

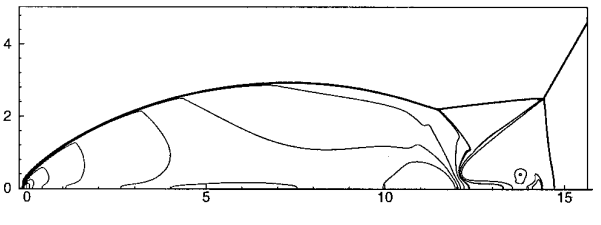

FIG. 11. Density contours for an $M = 9.5$ shock reflection at a $\alpha = 30°$ wedge using the implicit EFM method.

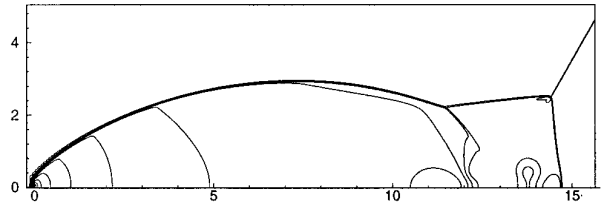

FIG. 12. Pressure contours for an $M = 9.5$ shock reflection at a $\alpha = 30°$ wedge, using the implicit EFM method.

meshes, ω can take larger values. At present, we do not have any prescription for ω, except that its value is problem dependent and chosen essentially by trial and error to get the best possible convergence rates.

We compute this problem using both the implicit Godunov method and the implicit EFM method. The contour plots of the density and pressure for each of these methods are shown in Figs. 11–14. It is well known for a Godunov

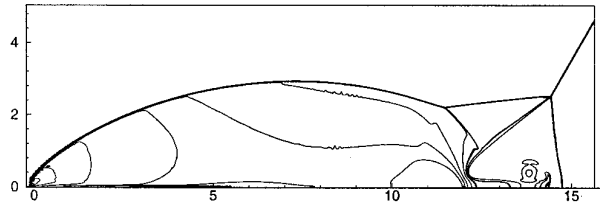

FIG. 13. Density contours for an $M = 9.5$ shock reflection at a $\alpha = 30°$ wedge using the implicit Godunov method.

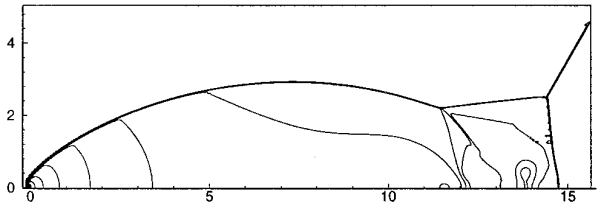

FIG. 14. Pressure contours for an $M = 9.5$ shock reflection at a $\alpha = 30°$ wedge using the implicit Godunov method.

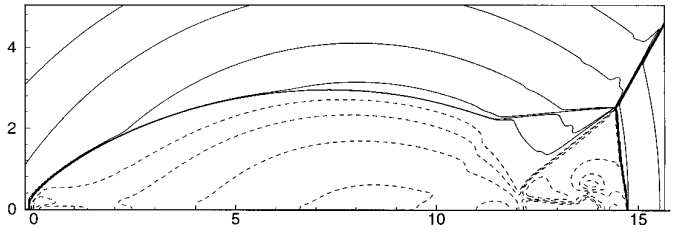

FIG. 15. Self-similar Mach number, $\tilde{M} \in (0.0, 12.3)$, for the 2D reflection problem using the implicit EFM method. The subsonic contours are shown as dashed lines.

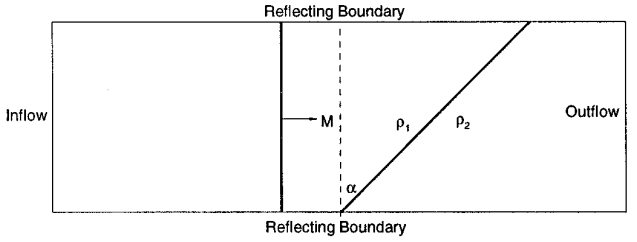

FIG. 16. Schematic of a two-dimensional shock contact-discontinuity interaction.

method that a slowly moving shock which is nearly aligned with the grid will exhibit numerical oscillations in the transverse direction. In this case the slightly curved Mach stem is nearly aligned with the grid and moves slowly on the mesh while converging to a steady configuration in the self-similar coordinates. These transverse oscillations are clearly present and are in fact visible in the pressure (see Fig. 14). The implicit EFM method gives equally good quality results (Figs. 11–12) and, in addition, is devoid of the aforementioned numerical oscillations. At convergence, the L_∞ norm of the residual was less than 10^{-10}. It is interesting to examine the self-similar Mach number defined by Eq. (14). For this case, the contours of $\tilde{M}$ are plotted in Fig. 15 with the dashed (solid) contours for subsonic (supersonic) $\tilde{M}$ indicating regions of elliptic (hyperbolic) nature of the equations.

B. *Shock-Refraction*

In this section, we compute the solution of a shock wave refraction at an oblique gaseous interface. The physical situation may be characterized by a shock wave moving from left to right and interacting with the inclined contact-discontinuity (see Fig. 16). As long as the shock continues to traverse the interface, the solution is self-similar. We compute the specific case of a $M = 2.02$ shock interaction with the initially stationary contact-discontinuity inclined at an angle $\alpha = 60°$ to the plane of the shock. The pressure on either side of the contact-discontinuity is unity while

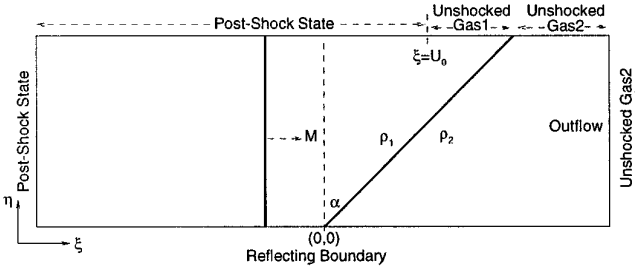

FIG. 17. Boundary conditions and initial guess for the two-dimensional shock contact-discontinuity interaction.

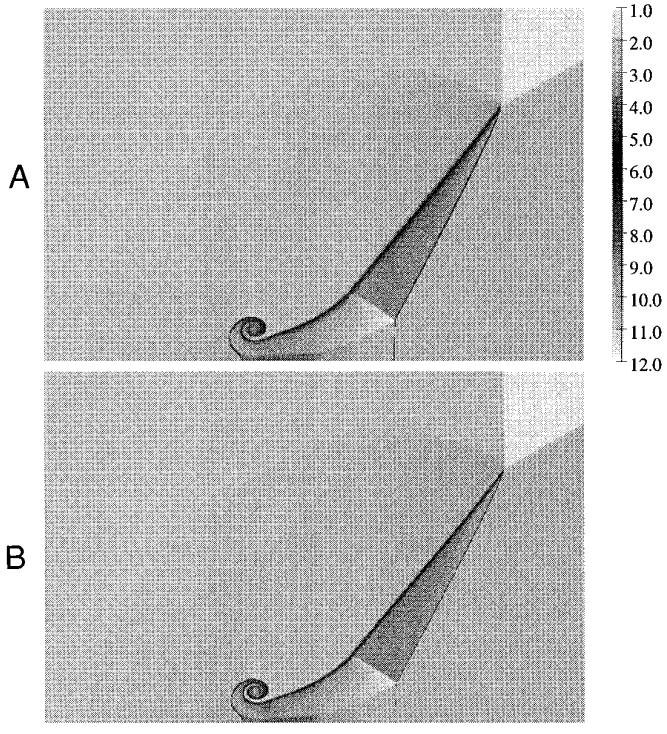

FIG. 18. Density images for self-similar solution of the shock refraction process using the implicit Godunov method. Grid sizes: (A) 768 × 392 and (B) 1536 × 768.

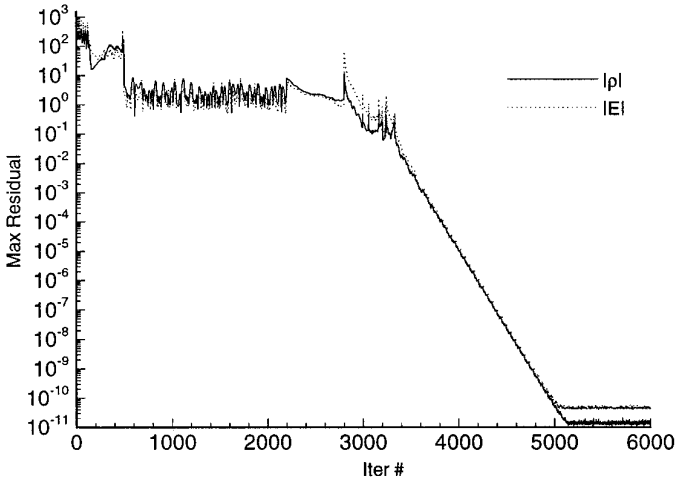

FIG. 19. Maximum residual for the continuity and the energy equation for the self-similar problem using the implicit Godunov method. The grid size is 1536 × 768.

the density is $\rho = 1$ ($\rho = 3$) to the left (right). For the self-similar solution the boundary conditions and the initial guess are shown in Fig. 17.

We employ two mesh sizes: (A) ''coarse''—768 × 384 and (B) ''fine''—1536 × 768. For the implicit Godunov method, gray-scale density images are shown for the self-similar computation (Fig. 18). The convergence history for the fine mesh computation is shown in Fig. 19. The contours of $\tilde{M}$ are plotted in Fig. 20 and indicate regions of ellipticity and hyperbolicity of the equations.

For the fine mesh, we also computed the solution using implicit EFM. We examine a magnified juxtaposition of the self-similar solutions obtained by the implicit Godunov and implicit EFM in Fig. 21. Note the implicit Godunov solution has been reflected about the ξ axis. Qualitatively the two solutions look similar. A quantitative comparison between the two methods is made by comparing the density and pressure cross-sections taken at locations A–F in Fig. 21. These density and pressure cross-sections are shown in Figs. 22 and 23.

A region of interest is the rolled up vortex sheet (actually a vortex layer) near the lower wall. The cross-sections A–D are taken through this structure. While the pressure profiles show marked similarity between the implicit Godunov and implicit EFM, the density cross-sections show a better resolution by the implicit Godunov method. It is ambiguous whether this roll-up should have an infinite number of turns.

Clearly the Mach stem (cross-section F) is very sharply resolved by both the methods. The contact discontinuity at cross-section E is spread over several computational zones as seen in Fig. 22, while the pressure profile is continuous and in fact almost constant across the contact discontinuity at location E as seen in Fig. 23.

1. *Comparison with Initial-Value Computations.* Juxtaposition of initial value and the self-similar solutions (which have been reflected about the ξ axis) for the coarse and fine meshes are shown in Fig. 24 and Fig. 25, respectively. The initial value problem was solved until time $t = 1$ for both meshes. It is well known that baroclinic generation of circulation occurs at the shocked contact discontinuity [13] and so the shocked contact discontinuity is a vortex sheet. Linear stability analysis of a vortex sheet in compressible inviscid flow indicates instability if the convective

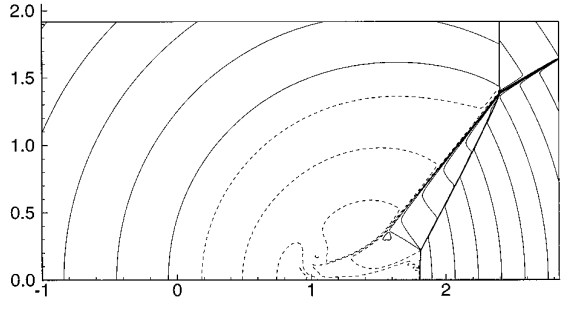

FIG. 20. Self-similar Mach number, $\tilde{M} \in (0.0, 4.79)$, for the 2D refraction problem using the implicit Godunov Method. The subsonic contours are shown as dashed lines.

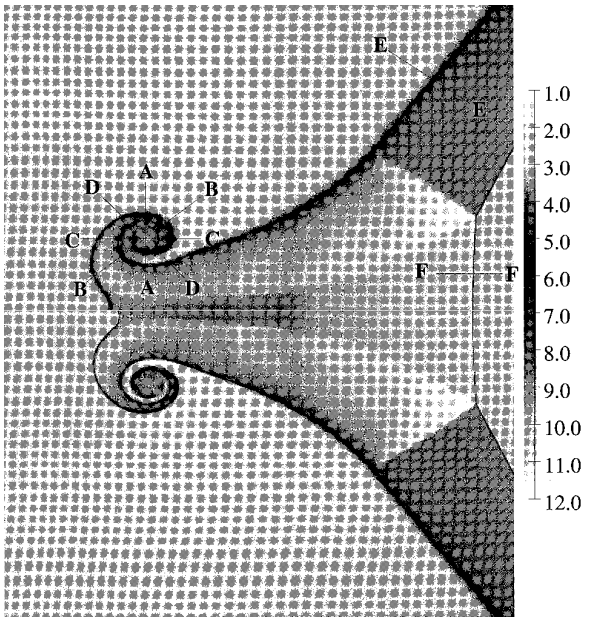

FIG. 21. A juxtaposition of the density for the self-similar solution. The top half is computed using implicit EFM while the lower half is computed using the implicit Godunov method. The implicit Godunov solution has been reflected about the ξ-axis. The grid size is 1536×768. A through F mark the cross-sections shown in the next two figures.

Mach number (M_c) is less than unity [15]. In our specific case, M_c is approximately 0.3 (see Ref. [13] to estimate M_c) and hence the shocked contact discontinuity is a linearly unstable vortex sheet. Thus disturbances introduced at the grid level grow with time in the initial-value computation. While absent or small for the coarse mesh, manifestations of the Kelvin–Helmholtz instability are clearly seen for the fine mesh in the neighborhood of the contact discontinuity for the initial-value solution. On the other hand, the self-similar solution is devoid of the Kelvin–Helmholtz instability for both the coarse and the fine mesh. Since the vortex sheet is linearly unstable, the self-similar solution may be interpreted to be a solution of the compressible Euler equations residing on an unstable manifold in some function space. Samtaney and Pullin [16] have conjectured on the nature of the initial-value solution and the self-similar solution when vortex sheets are present, in the limit of zero mesh spacing.

VI. CONCLUSION

In this paper, we expressed the Euler equations as a system of hyperbolic-elliptic partial differential equations by employing the self-similar ($\xi \equiv x/t$, $\eta = \equiv y/t$) transformation. We then developed two methods to numerically obtain the self-similar solutions of the compressible Euler equations as a boundary value problem. One of the methods was explicit while the other was implicit. For each of these methods we employed either the Godunov technique or the Equilibirum Flux Method to compute the fluxes. For the implicit Godunov method and the implicit Equilibrium Flux Method, the Jacobians were derived analytically. These Jacobians are not only useful for the restricted class of self-similar solution but have a wider applicability. For instance, if one were to solve the initial value problem (3) with an implicit method, we would need still the Jacobian of the fluxes. In this case, the Jacobians of the fluxes (either for the Godunov method or EFM) may be used if one simply substitutes $\xi = 0$, $\eta = 0$ in the analysis in Appendixes A and B.

Two-dimensional flows which exhibit self-similar solutions such as shock reflection at a solid wedge or shock refraction at a gaseous interface or shock diffraction over a right angle corner are intuitively easier to comprehend by examining the self-similar solution than a time-dependent one because the number of independent variables in the self-similar formulation is one less than the initial-value formulation. Comparison of the implicit EFM and the implicit Godunov method, in the context of the two-dimensional refraction problem, suggests that these two completely diverse methods of computing the fluxes still yield similar results albeit the EFM solution is more diffusive than the Godunov method.

Another clear advantage of the self-similar approach is that, in general, in the self-similar solution the resolution of the discontinuities is sharper than the corresponding initial-value solution. This is evident from an examination of the self-similar solution of the Sod's shock-tube problem and the one-dimensional shock refraction problem, both of which exhibit a very sharp contact discontinuity.

Finally, we conclude by repeating the conjecture of Samtaney and Pullin [16] that the initial-value problem does not appear to converge to a weak solution as the mesh is refined, owing to illposedness in the neighborhood of the shocked contact discontinuity or the vortex sheet. In contrast, the self-similar solution seems to converge with decreasing mesh spacing to a weak solution, which we believe exists and is unique, although we note there are no existence and uniqueness proofs for multi-dimensional compressible Euler equations. Thus, one may think of the self-similar solution as residing on some unstable manifold or as a basic state which is unstable.

APPENDIX A: JACOBIAN FOR THE IMPLICIT GODUNOV METHOD

Consider a cell interface $\hat{\xi} = constant$. In the Godunov method the flux F depends upon the left and right states, U_L and U_R, at the cell interface, i.e., $F \equiv F(U_L, U_R)$,

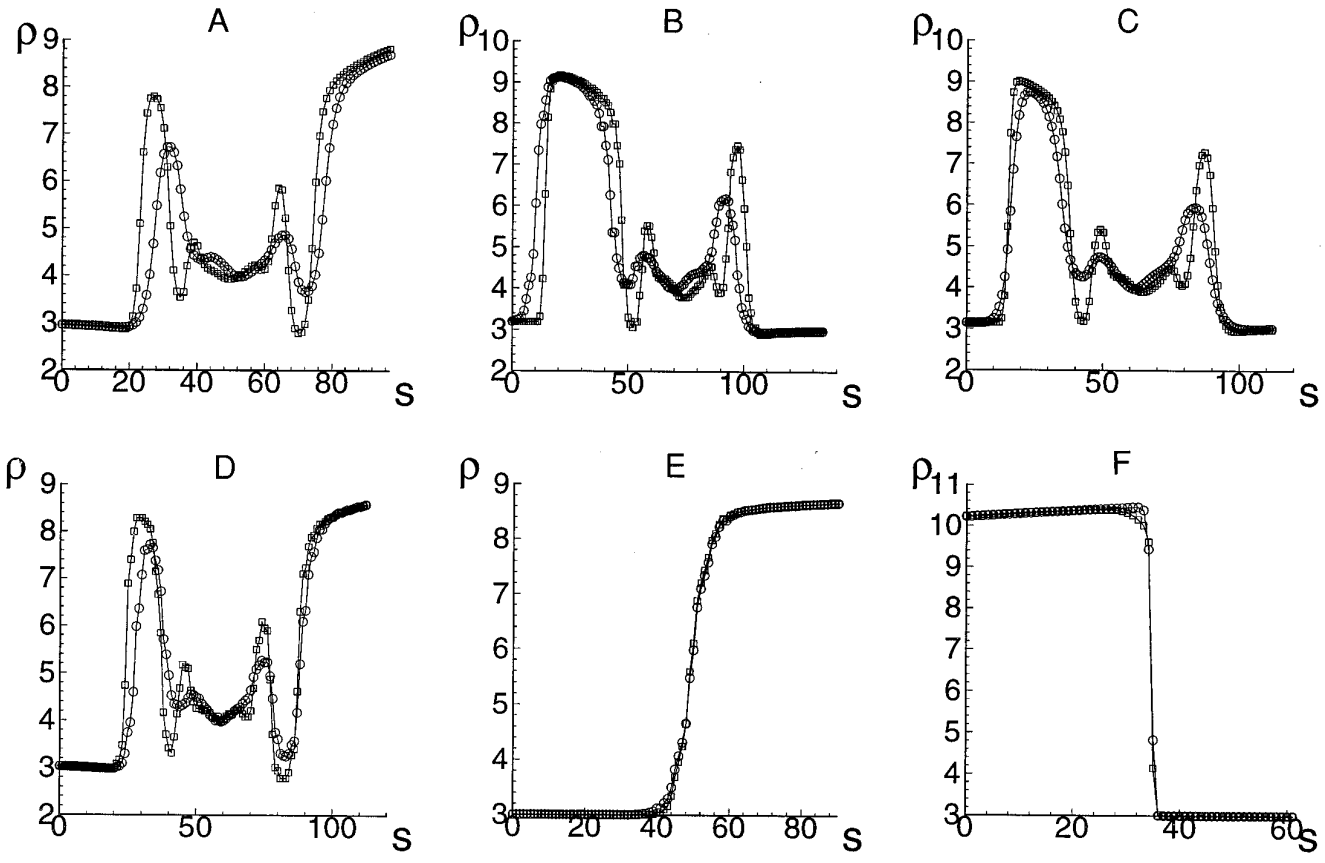

FIG. 22. Cross-sections of density for the 2D refraction problem. Circles (squares) indicate implicit EFM (implicit Godunov method).

and is determined by solving a one-dimensional Riemann problem exactly. We seek the Jacobian of F with respect to U_L and U_R. The solution to the Riemann problem is itself a self-similar solution, i.e., it depends only upon $\xi = x/t$. Let $W(\xi)$ be the solution to the Riemann problem. Note that F in the self-similar formulation is equivalent to the flux of mass, momentum, and energy through an interface whose speed itself is $\hat{\xi}$ (see Eq. (7)). Therefore, it is appropriate to use the solution of the Riemann problem along $\hat{\xi}$ to compute the flux F. Thus, $F \equiv F(U_L, U_R) \equiv F(W(\hat{\xi}))$.

The solution to the Riemann problem consists of two genuinely nonlinear waves (denoted as the 1-wave and 3-wave) and one linearly degenerate contact discontinuity (denoted as the 2-wave). There are four possible combinations of the nonlinear waves: (a) $S_1 - S_3$, (b) $S_1 - R_3$, (c) $R_1 - R_3$, and (d) $R_1 - S_3$ where S_1, S_3 are respectively a 1-shock and a 3-shock while R_1, R_3 are respectively a 1-rarefaction and 3-rarefaction wave [17]. The case of $R_1 - S_3$ is schematically depicted in Fig. 26. Let $W_{s,k}$, $k = 1, 3$, denote the speed of the 1-shock and 3-shock. Let $U_{h,k}$ and $U_{t,k}$, $k = 1, 3$, denote the speeds of the head and tail of the rarefaction, respectively. In evaluating the solution to the Riemann problem it is convenient to consider the variables (ρ, u, p) since u and p are continuous across the 2-wave and only a jump in the density occurs across the 2-wave. The Riemann data are $Q_L = \{\rho_L, u_L, p_L\}^T$ and $Q_R = \{\rho_R, u_R, p_R\}^T$. We denote the two constant states in the solution by $Q_L^* = \{\rho_L^*, u^*, p^*\}^T$ and $Q_R^* = \{\rho_R^*, u^*, p^*\}^T$. For the 1-rarefaction we have a continuum of constant states bounded between the $U_{h,1} = u_L - c_L$ and $U_{t,1} = u^* - c_L^*$ characteristics. Likewise the states within the 3-rarefaction are bounded by the curves $U_{h,3} = u_R + c_R$ and $U_{t,3} = u^* + c_R^*$. We denote the states within the 1-rarefaction and the 3-rarefaction by $\tilde{Q}_1 = \{\tilde{\rho}_1, \tilde{u}_1, \tilde{p}_1\}^T$ and $\tilde{Q}_3 = \{\tilde{\rho}_3, \tilde{u}_3, \tilde{p}_3\}^T$, respectively.

We solve the Riemann problem by a Newton–Raphson technique. For further detail on the solution to the Riemann problem, see the extensive discussion in Refs. [17, 18]. Table II gives the solution vector W at the location $\hat{\xi}$.

The procedure to calculate the Jacobian A of F with respect to U_K, $K = L, R$, follows.

$$A \equiv \left(\frac{\partial F}{\partial U_K}\right). \tag{A1}$$

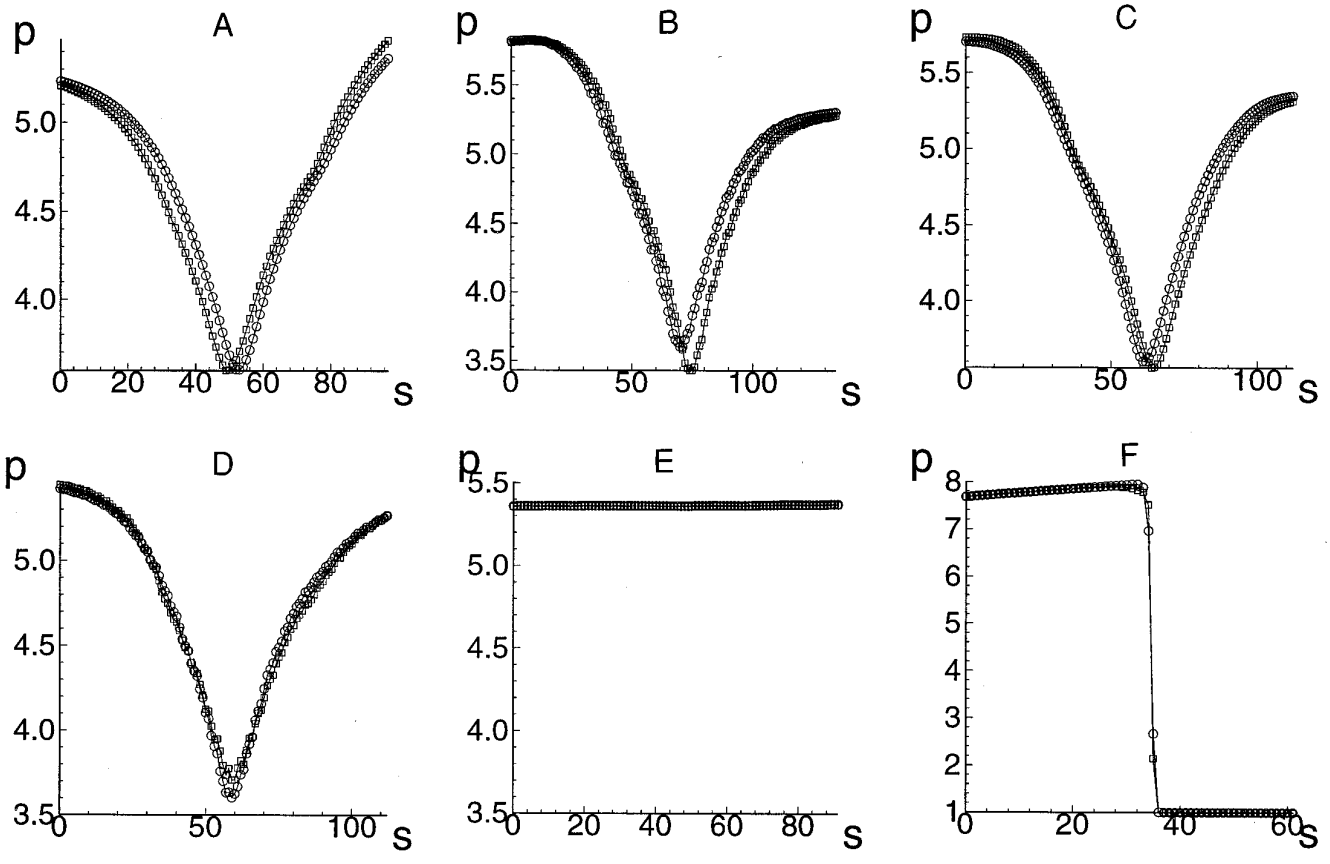

FIG. 23. Cross-sections of pressure for the 2D refraction problem. Circles (squares) indicate implicit EFM (implicit Godunov method).

We rewrite A as

$$A = \left(\frac{\partial F}{\partial W}\right)\left(\frac{\partial W}{\partial Q_K}\right)\left(\frac{\partial Q_K}{\partial U_K}\right), \tag{A2}$$

where

$$W = \{\rho, u, v, p\}^T, \tag{A3}$$

$$Q_K = \{\rho_k, u_k, v_k, p_k\}^T, \tag{A4}$$

$$U_K = \{\rho_k, \rho_k u_k, \rho_k v_k, E_k\}^T. \tag{A5}$$

It is straightforward to derive the first and third terms in the above product of Jacobians. These are

$$\frac{\partial F}{\partial W} = \begin{bmatrix} u-\hat{\xi} & \rho & 0 & 0 \\ u(u-\hat{\xi}) & \rho(2u-\hat{\xi}) & 0 & 1 \\ (u-\hat{\xi})v & \rho v & \rho(u-\hat{\xi}) & 0 \\ \frac{q^2}{2}(u-\hat{\xi}) & \frac{q^2}{2}+\rho u(u-\hat{\xi})+\frac{\gamma}{\gamma-1}p & \rho v(u-\hat{\xi}) & \frac{\gamma u-\hat{\xi}}{\gamma-1} \end{bmatrix}, \tag{A6}$$

where $q^2 = u^2 + v^2$, and

$$\frac{\partial Q_K}{\partial U_K} = \begin{bmatrix} 1 & 0 & 0 & 0 \\ -\frac{u_K}{\rho_K} & \frac{1}{\rho_K} & 0 & 0 \\ -\frac{v_K}{\rho_K} & 0 & \rho_K v_K & 0 \\ (\gamma-1)\frac{q_K^2}{2} & -(\gamma-1)u_K & -(\gamma-1)v_K & (\gamma-1) \end{bmatrix}, \tag{A7}$$

where $q_K^2 = u_K^2 + v_K^2$.

Consider the entries in the Jacobians $\partial W/\partial Q_K$, $K = L$, R. If $W(\hat{\xi}) = Q_L$ ($W(\hat{\xi}) = Q_R$) then the Jacobian is trivially given by

$$\left(\frac{\partial W}{\partial Q_L}\right) = I(0), \qquad \left(\frac{\partial W}{\partial Q_R}\right) = 0(I). \tag{A8}$$

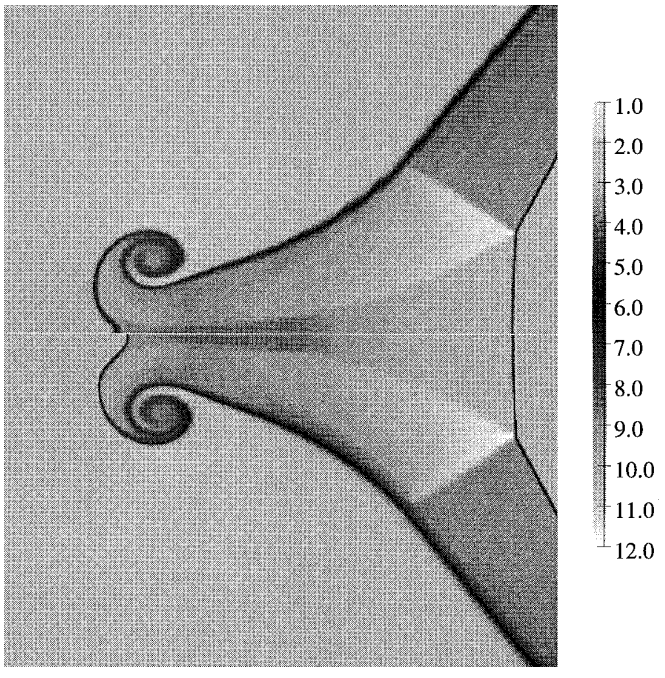

FIG. 24. A zoom of juxtaposition of the density for unsteady solution and the self-similar solution. The grid size is 768 × 384. The self-similar solution obtained by the implicit Godunov method has been reflected about the ξ-axis.

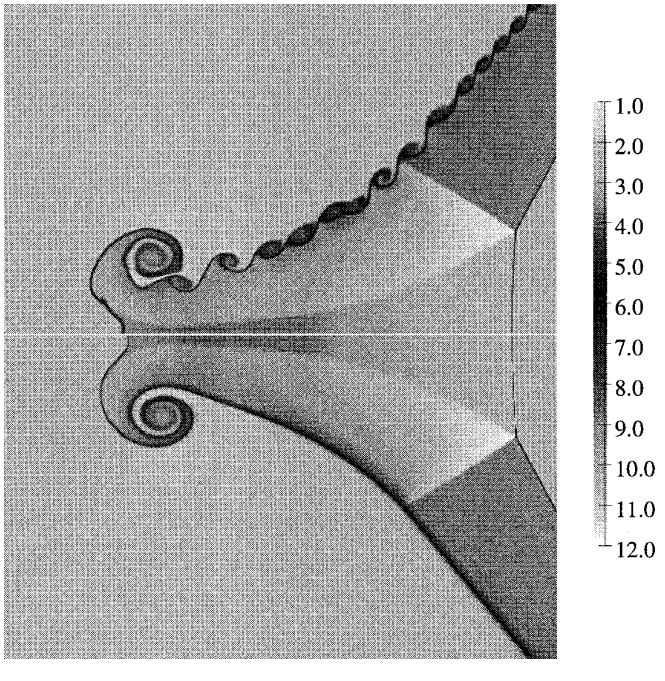

FIG. 25. A zoom of juxtaposition of the density for unsteady solution and the self-similar solution. The grid size is 1536 × 768. The self-similar solution obtained by the implicit Godunov method has been reflected about the ξ-axis.

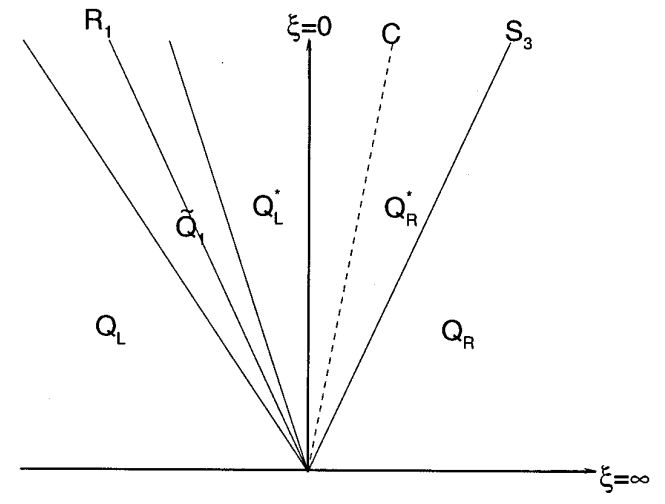

FIG. 26. Solution to the Riemann problem has four combinations of the genuinely nonlinear waves. In this schematic the 1-wave is a rarefaction R_1, and the 3-wave is a shock S_3. The linearly degenerate wave or the contact-discontinuity is depicted as C.

If $W = Q_L^*$ then the Jacobian is given by

$$\frac{\partial W}{\partial Q_K} = \begin{bmatrix} \frac{\partial \rho_L^*}{\partial \rho_K} & \frac{\partial \rho_L^*}{\partial u_K} & \frac{\partial \rho_L^*}{\partial v_K} & \frac{\partial \rho_L^*}{\partial p_K} \\ \frac{\partial u^*}{\partial \rho_K} & \frac{\partial u^*}{\partial u_K} & \frac{\partial u^*}{\partial v_K} & \frac{\partial u^*}{\partial p_K} \\ \frac{\partial v^*}{\partial \rho_K} & \frac{\partial v^*}{\partial u_K} & \frac{\partial v^*}{\partial v_K} & \frac{\partial v^*}{\partial p_K} \\ \frac{\partial p^*}{\partial \rho_K} & \frac{\partial p^*}{\partial u_K} & \frac{\partial p^*}{\partial v_K} & \frac{\partial p^*}{\partial p_K} \end{bmatrix}. \tag{A9}$$

If $W = Q_R^*$ then replace ρ_L^* in the first row above by ρ_R^*. If $W = \tilde{Q}_1$ or $W = \tilde{Q}_3$ then replace (ρ_L, u^*, v^*, p^*) by $(\tilde{\rho}_l, \tilde{u}_l, \tilde{v}_l, \tilde{p}_l)$ where $l = 1, 3$ depending upon whether $W = \tilde{Q}_1$ or $W = \tilde{Q}_3$.

Note that the tangential velocity, v, in the solution to the Riemann problem is chosen to be $v^* = v_L$ ($v^* = v_R$) if $u^* > \hat{\xi}$ ($u^* < \hat{\xi}$). All the entries in the Jacobian involving the derivative of the tangential velocity with respect to the density, normal velocity, and pressure are then zero. The entries in the Jacobian which are the derivative of v^* with respect to v_K are then

$$\frac{\partial v^*}{\partial v_K} = 0(1), \qquad K = L(R) \text{ if } u^* < \hat{\xi}, \tag{A10}$$

$$\frac{\partial v^*}{\partial v_K} = 1(0), \qquad K = L(R) \text{ if } u^* > \hat{\xi}. \tag{A11}$$

TABLE II

Solution of the Riemann Problem at $\hat{\xi}$

$W(\hat{\xi})$	$S_1 - S_3$	$S_1 - R_3$	$R_1 - R_3$	$R_1 - S_3$
Q_L	$\hat{\xi} < W_{s,1}$	$\hat{\xi} < W_{s,1}$	$\hat{\xi} < U_{h,1}$	$\hat{\xi} < U_{h,1}$
Q_R	$\hat{\xi} > W_{s,3}$	$\hat{\xi} > U_{h,3}$	$\hat{\xi} > U_{h,3}$	$\hat{\xi} > W_{s,3}$
Q_L^*	$W_{s,1} < \hat{\xi} < u^*$	$W_{s,1} < \hat{\xi} < u^*$	$U_{t,1} < \hat{\xi} < u^*$	$U_{t,1} < \hat{\xi} < u^*$
Q_R^*	$u^* < \hat{\xi} < W_{s,3}$	$u^* < \hat{\xi} < U_{t,3}$	$u^* < \hat{\xi} < U_{t,3}$	$u^* < \hat{\xi} < W_{s,3}$
$\tilde{Q}_1$	—	—	$U_{h,1} < \hat{\xi} < U_{t,1}$	$U_{h,1} < \hat{\xi} < U_{t,1}$
$\tilde{Q}_3$	—	$U_{t,3} < \hat{\xi} < U_{h,3}$	$U_{t,3} < \hat{\xi} < U_{h,3}$	—

Note. The execution time is given in seconds for the Intel Paragon. The number in the bracket is the speed-up which is normalized to unity for four processors.

The other entries in the Jacobian are found by solving a linearly perturbed Riemann problem described below.

1. Linearly Perturbed Riemann Problem

Let the left and right states be perturbed infinitesimally to $Q_L + Q'_L = (\rho_L + \rho'_L, u_L + u'_L, p_L + p'_L)$ and $Q_R + Q'_R = (\rho_R + \rho'_R, u_R + u'_R, p_R + p'_R)$. We seek the perturbed solution by linearizing about the unperturbed solution to the Riemann problem. Let the perturbed solution in the constant regions between the nonlinear waves and the 2-wave be $Q_L^* + Q_L^{*\prime} = (\rho_L^* + \rho_L^{*\prime}, u^* + u^{*\prime}, p^* + p^{*\prime})$ and $Q_R^* + Q_{R^{*\prime}} = (\rho_R^* + \rho_R^{*\prime}, u^* + u^{*\prime}, p^* + p^{*\prime})$. Consider each nonlinear wave separately.

a. *1-Rarefaction R_1*

For the unperturbed solution, writing the Riemann invariant and the isentropic conditions gives us the equations

$$u^* + \frac{2}{\gamma - 1} c_L^* = u_L + \frac{2}{\gamma - 1} c_L, \tag{A12}$$

$$\frac{p^*}{\rho^{*\gamma}} = \frac{p_L}{\rho_L^{\gamma}}. \tag{A13}$$

For the perturbed solution, we get

$$u^* + u^{*\prime} + \frac{2}{\gamma - 1}(c^* + c^{*\prime}) = u_L + u'_L + \frac{2}{\gamma - 1}(c_L + c'_L), \tag{A14}$$

$$\frac{p^* + p^{*\prime}}{(\rho_L^* + \rho_L^{*\prime})^{\gamma}} = \frac{p_L + p'_L}{(\rho_L + \rho'_L)^{\gamma}}. \tag{A15}$$

Linearizing we get

$$\begin{aligned} &- \frac{c_L^*}{(\gamma - 1)\rho_L^*} \rho_L^{*\prime} + u^{*\prime} + \frac{c_L^*}{(\gamma - 1)p^*} p^{*\prime} \\ &\quad = - \frac{c_L}{(\gamma - 1)\rho_L} \rho'_L + u'_L + \frac{c_L}{(\gamma - 1)p_L} p'_L, \\ &\quad - \frac{\gamma p^*}{\rho_L^{*(\gamma+1)}} \rho_L^{*\prime} + \frac{1}{\rho_L^{*\gamma}} p^{*\prime} = \frac{\gamma p_L}{\rho_L^{\gamma+1}} \rho'_L + \frac{1}{\rho_L^{\gamma}} p'_L. \end{aligned} \tag{A16}$$

b. *3-Rarefaction R_3*

The same equations hold as for the above case, except that the second term in the Riemann invariant equation has the opposite sign. The linearized equations are

$$\begin{aligned} &\frac{c_R^*}{(\gamma - 1)\rho_R^*} \rho_R^{*\prime} + u^{*\prime} - \frac{c_R^*}{(\gamma - 1)p^*} p^{*\prime} \\ &\quad = \frac{c_R}{(\gamma - 1)\rho_R} \rho'_R + u'_R - \frac{c_R}{(\gamma - 1)p_R} p'_R, \\ &\quad - \frac{\gamma p^*}{\rho_R^{*(\gamma+1)}} \rho_R^{*\prime} + \frac{1}{\rho_R^{*\gamma}} p^{*\prime} = - \frac{\gamma p_R}{\rho_R^{\gamma+1}} \rho'_R + \frac{1}{\rho_R^{\gamma}} p'_R. \end{aligned} \tag{A17}$$

c. *1-Shock S_1*

For a 1-shock, the following three jump conditions hold for the unperturbed solution,

$$\rho_L^*(u^* - W_{s,1}) = \rho_L(u_L - W_{s,1}), \tag{A18}$$

$$p^* + \rho_L^*(u^* - W_{s,1})^2 = p_L + \rho_L(u_L - W_{s,1})^2, \tag{A19}$$

$$h_L^* + \frac{1}{2}(u^* - W_{s,1})^2 = h_L + \frac{1}{2}(u_L - W_{s,1})^2, \tag{A20}$$

where $h = \gamma p/(\gamma - 1)\rho$ is the enthalpy for a perfect gas. Upon perturbation the jump conditions become

$$(\rho_L^* + \rho_L^{*\prime})(u^* + u^{*\prime} - W_{s,1} - W'_{s,1}) = (\rho_L + \rho'_L)(u_L + u'_L - W_{s,1} - W'_{s,1}), \quad \text{(A21)}$$

$$p^* + p^{*\prime} + (\rho^* + \rho^{*\prime})(u^* + u^{*\prime} - W_{s,1} - W'_{s,1})^2 = p_L + p'_L + (\rho_L + \rho'_L)(u_L + u'_L - W_{s,1} - W'_{s,1})^2, \quad \text{(A22)}$$

$$h_L^* + h_L^{*\prime} + \frac{1}{2}(u^* + u^{*\prime} - W_{s,1} - W'_{s,1})^2 = h_L + h'_L + \frac{1}{2}(u_L + u'_L - W_{s,1} - W'_{s,1})^2. \quad \text{(A23)}$$

In the above equations $W'_{s,1}$ is the perturbation to the shock speed. Linearizing the above equations and eliminating $W'_{s,1}$ and the enthalpy terms by using the thermodynamic relation for enthalpy we get the linear equations.

$$\begin{aligned}
&(u^* - W_{s,1})^2\rho_L^{*\prime} + 2\rho_L^*(u^* - W_{s,1})u^{*\prime} + p^{*\prime} \\
&= (u_L - W_{s,1})^2\rho'_L + 2\rho_L(u_L - W_{s,1})u'_L + p'_L, \\
&\left(-\frac{\gamma}{(\gamma-1)}\frac{p^*(\rho_L - \rho_L^*)}{\rho_L^{*2}}\right)\rho_L^{*\prime} \\
&+ ((\rho_L - \rho_L^*)(u^* - W_{s,1}) - \rho_L^*(u_L - u^*))u^{*\prime} \\
&+ \left(\frac{\gamma}{(\gamma-1)}\frac{(\rho_L - \rho_L^*)}{\rho_L^*}\right)p^{*\prime} \\
&= \left(-\frac{\gamma}{(\gamma-1)}\frac{p_L(\rho_L - \rho_L^*)}{\rho_L^2}\right)\rho'_L \\
&+ ((\rho_L - \rho_L^*)(u_L - W_{s,1}) - \rho_L(u_L - u^*))u'_L, \\
&+ \left(\frac{\gamma}{(\gamma-1)}\frac{(\rho_L - \rho^*)}{\rho_L}\right)p'_L.
\end{aligned} \quad \text{(A24)}$$

d. *3-Shock S_3*

For a 3-shock, the linearized equations are

$$\begin{aligned}
&(u^* - W_{s,3})^2\rho_R^{*\prime} + 2\rho_R^*(u^* - W_{s,3})u^{*\prime} + p^{*\prime} \\
&= (u_R - W_{s,3})^2\rho'_R + 2\rho_L(u_R - W_{s,3})u'_L + p'_L, \\
&\left(-\frac{\gamma}{(\gamma-1)}\frac{p^*(\rho_R - \rho_R^*)}{\rho_R^{*2}}\right)\rho_R^{*\prime} \\
&+ ((\rho_R - \rho_R^*)(u^* - W_{s,3}) - \rho_R^*(u_R - u^*))u^{*\prime} \\
&+ \left(\frac{\gamma}{(\gamma-1)}\frac{(\rho_R - \rho_R^*)}{\rho_R^*}\right)p^{*\prime} \\
&= \left(-\frac{\gamma}{(\gamma-1)}\frac{p_L(\rho_L - \rho_R^*)}{\rho_R^2}\right)\rho'_R \\
&+ ((\rho_R - \rho_R^*)(u_R - W_{s,3}) - \rho_R(u_R - u^*))u'_R, \\
&+ \left(\frac{\gamma}{(\gamma-1)}\frac{(\rho_R - \rho_R^*)}{\rho_R}\right)p'_R.
\end{aligned} \quad \text{(A25)}$$

Once the nonlinear wave combination is determined to be one of the four choices, we have four linear equations in four unknowns namely, $\rho_L^{*\prime}$, $\rho_R^{*\prime}$, $u^{*\prime}$, $p^{*\prime}$. The above system of equations can be summarized as

$$[A](\rho_L^{*\prime}, u^{*\prime}, p^{*\prime})^T = [C](\rho'_L, u'_L, p'_L)^T, \quad \text{(A26)}$$

$$[B](\rho_R^{*\prime}, u^{*\prime}, p^{*\prime})^T = [D](\rho'_R, u'_R, p'_R)^T, \quad \text{(A27)}$$

where $[A]$, $[B]$, $[C]$, $[D]$ are 2×3 matrices. The elements of these matrices are the appropriate coefficients of $\rho_L^{*\prime}$, $\rho_R^{*\prime}$, $u^{*\prime}$, $p^{*\prime}$. Thus for example if the nonlinear wave combination was $R_1 - S_3$ then Eq. (A16) and Eq. (A25) can be written in the form of Eq. (A26) and Eq. (A27).

Solve for $(\rho_L^{*\prime}, \rho_R^{*\prime}, u^{*\prime}, p^{*\prime})$ by setting (ρ'_L, u'_L, p'_L) to (1, 0, 0), (0, 1, 0), and (0, 0, 1) in Eq. (A26) and setting the right hand side of Eq. (A27) to zero. Therefore, when $(\rho'_L, u'_L, p'_L) = (1, 0, 0)$ then the solution $(\rho_L^{*\prime}, \rho_R^{*\prime}, u^{*\prime}, p^{*\prime})$ represents the entries $(\partial\rho_L^{*\prime}/\partial\rho_L, \partial\rho_R^{*\prime}/\partial\rho_L, \partial u^{*\prime}/\partial\rho_L, \partial p^{*\prime}/\partial\rho_L)$ in the Jacobian $(\partial W/\partial Q_L)$.

Similarly, the Jacobian $(\partial W/\partial Q_R)$ is obtained by setting (ρ'_R, u'_R, p'_R) to (1, 0, 0), (0, 1, 0), and (0, 0, 1) in Eq. (A27), the right hand side of Eq. (A26) to zero, and solving for $(\rho_L^{*\prime}, \rho_R^{*\prime}, u^{*\prime}, p^{*\prime})$.

There are still two special cases which must be considered. These are the transonic rarefaction cases, i.e., cases for which $u - \hat{\xi}$ is equal in magnitude to the sound speed. The solution to the Riemann problem at $\hat{\xi}$ could very well lie within a 1-rarefaction or a 3-rarefaction. If $W(\hat{\xi})$ lies inside the 1-rarefaction, then using $\tilde{u}_1 - \hat{\xi} = \tilde{c}_1$ we get the following additional linear equations

$$-\frac{\gamma+1}{\gamma-1}\frac{\tilde{c}_1}{2\tilde{p}_1}\tilde{p}'_1 + \frac{\gamma+1}{\gamma-1}\frac{\tilde{c}_1}{2\tilde{p}_1}\tilde{p}'_1 = -\frac{c_L^*}{(\gamma-1)\rho_L^*}\rho_L^{*\prime} + u^{*\prime} - \hat{\xi} + \frac{c_L^*}{(\gamma-1)p^*}p^{*\prime}, \quad \text{(A28)}$$

$$-\frac{\gamma\tilde{p}_1}{\tilde{p}_1^{(\gamma+1)}}\tilde{p}'_1 + \frac{1}{\tilde{p}_1^{\gamma}}\tilde{p}'_1 = -\frac{\gamma p^*}{\rho_L^{*(\gamma+1)}}\rho_L^{*\prime} + \frac{1}{\rho_L^{*\gamma}}p^{*\prime}, \quad \text{(A29)}$$

$$\tilde{u}'_1 = \frac{\gamma-1}{\gamma+1}u^{*\prime} + \frac{c_L^*}{(\gamma+1)p^*}p^{*\prime} - \frac{c_L^*}{(\gamma+1)\rho_L^*}\rho_L^{*\prime}. \quad \text{(A30)}$$

These equations are solved for $\tilde{p}_1'$, $\tilde{u}_1'$, and $\tilde{p}_1'$ in terms of $\rho_L^{*\prime}$, $u^{*\prime}$, and $p^{*\prime}$. If $W(\hat{\xi})$ lies inside the 3-rarefaction, then using $\tilde{u}_3 - \hat{\xi} = -\tilde{c}_3$ we get the linear equations

$$\frac{\gamma+1}{\gamma-1}\frac{\tilde{c}_3}{2\tilde{p}_3}\tilde{p}_3 - \frac{\gamma+1}{\gamma-1}\frac{\tilde{c}_3}{2\tilde{p}_3}\tilde{p}_3' = \frac{c_R^*}{(\gamma-1)\rho_R^*}\rho_R^{*\prime} + u^{*\prime} - \hat{\xi} - \frac{c_R^*}{(\gamma-1)p^*}p^{*\prime}, \tag{A31}$$

$$-\frac{\gamma\tilde{p}_3}{\tilde{\rho}_3^{(\gamma+1)}}\tilde{\rho}_3' + \frac{1}{\tilde{\rho}_3^{\gamma}}\tilde{p}_3' = -\frac{\gamma p^*}{\rho_R^{*(\gamma+1)}}\rho_R^{*\prime} + \frac{1}{\rho_R^{*\gamma}}p^{*\prime}, \tag{A32}$$

$$\tilde{u}_3' = \frac{\gamma-1}{\gamma+1}u^{*\prime} - \frac{c_R^*}{(\gamma+1)p^*}p^{*\prime} + \frac{c_R^*}{(\gamma+1)\rho_R^*}\rho_R^{*\prime}. \tag{A33}$$

These equations are solved for $\tilde{p}_3'$, $\tilde{u}_3'$, and $\tilde{p}_3'$ in terms of $\rho_R^{*\prime}$, $u^{*\prime}$, and $p^{*\prime}$.

Among the implicit methods found in the literature we would like to bring to the notice of the reader the implicit-explicit Godunov method developed by Collins *et al.* [19]. In this implicit-explicit Godunov method, the flux function is a hybrid with the explicit part computed by the Godunov method and so their method does not involve the Jacobian of the Godunov flux function.

APPENDIX B: JACOBIAN FOR THE IMPLICIT EFM METHOD

The basic idea of the Equilibrium Flux Method [7] is as follows: in the limit of an infinite collision rate in the Boltzmann equation, the distribution of molecular velocities everywhere would tend asymptotically towards the equilibrium distribution determined by the total mass, momentum, and energy within a computational cell. If the velocity distribution were known to be the Maxwellian distribution then the fluxes of the conserved quantities could be calculated. In the EFM method, the flux F at a cell interface $\hat{\xi}$ is also a function of the left and right states at the cell boundary and is written as

$$F \equiv F(U_L, U_R) = F^+(U_L) + F^-(U_R), \tag{B1}$$

where $F^+(U)$ and $F^-(U)$ are given by

$$F^{\pm} = \begin{bmatrix} \rho\tilde{V}^{\pm}(\equiv F_1) \\ \rho u\tilde{V}^{\pm} + \dfrac{\rho c_p^2}{2}W^{\pm}(\equiv F_2) \\ \rho v\tilde{V}^{\pm} \\ \rho h_0\tilde{V}^{\pm} - \dfrac{1}{4}\rho c_p^3 D^{\pm} - \dfrac{1}{2}\hat{\xi}^2 F_1 + \hat{\xi}F_2 \end{bmatrix}, \tag{B2}$$

where

$$W^{\pm} = \frac{1 \pm erf((u-\xi)/c_p)}{2}, \tag{B3}$$

$$D^{\pm} = \pm\frac{1}{2\sqrt{\pi}}\exp\left((u-\hat{\xi})^2/c_p^2\right), \tag{B4}$$

$$\tilde{V} \pm = (u-\hat{\xi})W^{\pm} + c_p D^{\pm}, \tag{B5}$$

while h_0 is similar to the total enthalpy and is given by

$$h_0 = \frac{1}{2}\left((u-\hat{\xi})^2 + v^2\right) + \frac{\gamma}{2(\gamma-1)}c_p^2. \tag{B6}$$

c_p is the most probable speed, i.e.,

$$c_p = (2RT)^{1/2}, \tag{B7}$$

where R is the gas constant and T is the temperature.

Define $Q \equiv \{\rho, u, v, c_p\}^T$. It is convenient to express the Jacobian as (dropping the $\pm$ superscript)

$$\left(\frac{\partial F}{\partial U}\right) = \left(\frac{\partial F}{\partial Q}\right)\left(\frac{\partial Q}{\partial U}\right). \tag{B8}$$

The Jacobian $\left(\dfrac{\partial Q}{\partial U}\right)$ is

$$\frac{\partial Q}{\partial U} = \begin{bmatrix} 1 & 0 & 0 & 0 \\ -\dfrac{u}{\rho} & \dfrac{1}{\rho} & 0 & 0 \\ -\dfrac{v}{\rho} & 0 & \dfrac{1}{\rho} & 0 \\ \dfrac{c_p}{2\rho}\left((\gamma-1)\dfrac{(u^2+v^2)}{c_p^2} - 1\right) & -(\gamma-1)\dfrac{u}{\rho c_p} & -(\gamma-1)\dfrac{v}{\rho c_p} & \dfrac{(\gamma-1)}{\rho c_p} \end{bmatrix}. \tag{B9}$$

It can be shown that the Jacobian $(\partial F/\partial Q)$ is

$$\frac{\partial F}{\partial Q} = \begin{bmatrix} \tilde{V} & \rho W & 0 & \rho D \\ u\tilde{V} + \frac{c_p^2}{2} W & \rho(\tilde{V} + uW + c_p D) & 0 & \rho(c_p W + \hat{\xi} D) \\ v\tilde{V} & \rho v W & \rho\tilde{V} & 0 \\ f_{41} & f_{42} & f_{43} & f_{44} \end{bmatrix}. \tag{B10}$$

where

$$\begin{aligned} f_{41} &= h_0\tilde{V} - \frac{1}{4} c_p^3 D + \frac{1}{2}\hat{\xi} c_p^2 W, \\ f_{42} &= \rho u\tilde{V} + \rho h_0 W + \frac{1}{2}\rho(u + \hat{\xi}) c_p D, \\ f_{43} &= \rho v\tilde{V} \\ f_{44} &= \rho h_0 D + \frac{\gamma}{\gamma - 1}\rho c_p\tilde{V} \\ &\quad + \rho\hat{\xi} c_p W - \frac{3}{4}\rho c_p^2 D - \frac{1}{2}\rho(u^2 - \hat{\xi}^2)\, D. \end{aligned} \tag{B11}$$

We bring the reader's attention to the work of Moscheta and Pullin [20] who developed an implicit EFM in which they have derived the Jacobian of the EFM flux analytically. However, they did so in the context of finding solutions of the initial-value problem. Furthermore, they used the total enthalpy in their derivation while we use the total energy as our conserved variable.

APPENDIX C: LINEAR RECONSTRUCTION PROCEDURE

To achieve second order accuracy the following linear reconstruction procedure was adopted. We use the vector $V = \{\rho, u, v, p\}^T$ to obtain the left and right states at the cell interface $\xi_{i+1/2}$ as

$$\begin{aligned} V_L &= V_i + \frac{\Delta\xi}{2}\left(\frac{\partial V}{\partial \xi}\right)_i, \\ V_R &= V_{i+1} - \frac{\Delta\xi}{2}\left(\frac{\partial V}{\partial \xi}\right)_{i+1}. \end{aligned} \tag{C1}$$

The slope in cell i is given by

$$\left(\frac{\partial V}{\partial \xi}\right)_i = [\mathcal{L}]_i^{-1}\ \text{minmod}\,(\tilde{V}_i, \tilde{V}_{i+1}, \tilde{V}_{i-1}), \tag{C2}$$

where $\tilde{V}_{i+k} = [\mathcal{L}]_i V_{i+k}$, $k = -1, 0, 1$, is the projection of V onto the characteristic space, and the minmod function provides the slope limiting [21]. The matrix of left eigenvectors of the Jacobian $\partial F/\partial V$ is $[\mathcal{L}]$ given by

$$[\mathcal{L}] = \begin{bmatrix} 0 & \frac{\rho}{2} & 0 & -\frac{1}{2c} \\ c & 0 & 0 & -\frac{1}{c} \\ 0 & 0 & 1 & 0 \\ 0 & \frac{\rho}{2} & 0 & \frac{1}{2c} \end{bmatrix}. \tag{C3}$$

Given V_L, V_R the conserved quantities U_L, U_R at the left and right of the cell interface are trivially obtained.

ACKNOWLEDGMENTS

This work was supported in part by AFOSR Grant F49620-93-1-0338. This work arose from collaboration with Professor D. I. Pullin. Furthermore, the author benefited tremendously from detailed enlightening discussoins with Professor D. I. Pullin. Useful discussions with Professor D. I. Meiron and M. R. Meloon are gratefully acknowledged. This research was performed in part using the CSCC parallel computer system operated by Caltech on behalf of the Concurrent Supercomputing Consortium.

REFERENCES

1. L. F. Henderson, P. Colella, and E. G. Puckett, On the refraction of shock waves at a slow-fast gas interface, *J. Fluid Mech.* **224,** 1 (1991).
2. H. G. Hornung, Regular and Mach reflection of shock waves, *Ann. Rev. Fluid Mech.* **18,** 33 (1986).
3. D. M. Jones, P. M. E. Martin, and C. K. Thornhill, A note on the pseudo-stationary flow behind a shock diffracted or reflected at a corner, *Proc. R. Soc. London A* **209,** 238 (1951).
4. H. M. Glaz, P. Colella, I. I. Glass, and R. L. Deschambault, A numerical study of shock-wave reflection with experimental comparisons, *Proc. R. Soc. London A* **398,** 117 (1985).
5. P. Kutler and V. S. Vijaya Shankar, Diffraction of a shock wave by a compression corner. I. Regular reflection, *AIAA J.* **15**(2), 197 (1977).
6. G. A. Sod, A survey of several finite difference methods of systems of nonlinear hyperbolic conservation laws, *J. Comput. Phys.* **27,** 1 (1978).
7. D. I. Pullin, Direct simulation methods for compressible ideal gas flow, *J. Comput. Phys.* **34,** 231 (1980).
8. S. K. Godunov, Difference methods for the numerical solution of the equations of fluid dynamics, *Mat. Sb.* **47,** 271 (1959).
9. P. L. Roe, Approximate Riemann solvers, parameters vectors and difference schemes, *J. Comput. Phys.* **43,** 357 (1981).
10. P. Colella and P. R. Woodward, The piecewise parabolic method, *J. Comput. Phys.* **54,** 174 (1984).

11. C.-W. Shu and S. Osher, Efficient implementation of essentially non-oscillatory shock capturing schemes, II, *J. Comput. Phys.* **83,** 32 (1989).
12. B. Einfeldt, C. D. Munz, P. L. Roe, and B. Sjögreen, On Godunov-type methods near low densities, *J. Comput. Phys.* **92,** 273 (1991).
13. R. Samtaney and N. J. Zabusky, Circulation deposition on shock-accelerated planar and curved density-stratified interfaces: Models and scaling laws, *J. Fluid Mech.* **269,** 45 (1994).
14. M. J. Berger and P. Colella, Local adaptive mesh refinement for shock hydrodynamics, *J. Comput. Phys.* **82,** 64 (1989).
15. J. W. Miles, On the disturbed motion of a plane vortex sheet, *J. Fluid Mech.* **3,** 538 (1958).
16. R. Samtaney and D. I. Pullin, On initial-value and self-similar solutions of the compressible Euler equations, *Phys. Fluids* **8**(10), 2650 (1996).
17. J. Smoller, *Shock waves and reaction-diffusion equations,* in *A Series of Comprehensive Studies in Mathematics* (Springer-Verlag, New York/Berlin, 1982).
18. P. Colella and H. M. Glaz, Efficient solution algorithms for the Riemann problem for real gases, *J. Comput. Phys.* **59,** 264 (1985).
19. J. P. Collins, P. Colella, and H. M. Glaz, An unsplit implicit-explicit Godunov method for compressible gas dynamics, in *Computational Fluid Dynamics,* edited by Ch. Hirch *et al.* (Elsevier, New York, 1992), pp. 659–666.
20. J. M. Moscheta and D. I. Pullin, A robust low diffusive kinetic scheme for the Navier-Stokes equations, *J. Comput. Phys.,* in press.
21. B. Van Leer, Towards the ultimate conservative difference scheme. IV. A new approach to numerical convection, *J. Comput. Phys.* **23,** 276 (1977).